

Modeling, Simulation, and Fabrication of a Fully Integrated, Acid-stable, Scalable Solar-Driven Water-Splitting System

Karl Walczak,^[a, b] Yikai Chen,^[c] Christoph Karp,^[c] Jeffrey W. Beeman,^[a, b] Matthew Shaner,^[c] Joshua Spurgeon,^[c] Ian D. Sharp,^[a, d] Xenia Amashukeli,^[c] William West,^[c] Jian Jin,^[a, e] Nathan S. Lewis,^{*, [c, f]} and Chengxiang Xiang^{*, [c]}

A fully integrated solar-driven water-splitting system comprised of $\text{WO}_3/\text{FTO}/\text{p}^+\text{n}$ Si as the photoanode, $\text{Pt}/\text{TiO}_2/\text{Ti}/\text{n}^+\text{p}$ Si as the photocathode, and Nafion as the membrane separator, was simulated, assembled, operated in 1.0 M HClO_4 , and evaluated for performance and safety characteristics under dual side illumination. A multi-physics model that accounted for the performance of the photoabsorbers and electrocatalysts, ion transport in the solution electrolyte, and gaseous product crossover was first used to define the optimal geometric design space for the system. The photoelectrodes and the membrane separators were then interconnected in a louvered design system configuration, for which the light-absorbing area and the solution-transport pathways were simultaneously optimized. The performance of the photocathode and the photoanode were separately evaluated in a traditional three-electrode photoelectrochemical cell configuration. The photocathode and photoanode were then assembled back-to-back in a tandem configuration to provide sufficient photovoltage

to sustain solar-driven unassisted water-splitting. The current-voltage characteristics of the photoelectrodes showed that the low photocurrent density of the photoanode limited the overall solar-to-hydrogen (STH) conversion efficiency due to the large band gap of WO_3 . A hydrogen-production rate of 0.17 mL hr^{-1} and a STH conversion efficiency of 0.24% was observed in a full cell configuration for $> 20 \text{ h}$ with minimal product crossover in the fully operational, intrinsically safe, solar-driven water-splitting system. The solar-to-hydrogen conversion efficiency, η_{STH} , calculated using the multiphysics numerical simulation was in excellent agreement with the experimental behavior of the system. The value of η_{STH} was entirely limited by the performance of the photoelectrochemical assemblies employed in this study. The louvered design provides a robust platform for implementation of various types of photoelectrochemical assemblies, and can provide an approach to significantly higher solar conversion efficiencies as new and improved materials become available.

Introduction

Interest in the development of solar-fuel generators began with the pioneering research of Fujishima and Honda in the early 1970s.^[1,2] The primary components of a solar-fuel generator include photoabsorbers, electrocatalysts, membrane separators, electrolytes, and the supporting structures. The photo-

absorbers capture and convert the incident photons into energetic electrons and holes, to provide the voltage and current for the fuel-forming reactions. The electrocatalysts lower the kinetic overpotentials and effect the efficient, stable, and selective fuel-forming reactions. The membrane separators prevent

[a] K. Walczak, J. W. Beeman, I. D. Sharp, J. Jin
Joint Center for Artificial Photosynthesis
Lawrence Berkeley National Laboratory
Berkeley, CA 94720 (USA)

[b] K. Walczak, J. W. Beeman
Materials Sciences Division
Lawrence Berkeley National Laboratory
Berkeley, CA 94720 (USA)

[c] Y. Chen, C. Karp, M. Shaner, J. Spurgeon,⁺ X. Amashukeli, W. West,
N. S. Lewis, C. Xiang
Joint Center for Artificial Photosynthesis
California Institute of Technology
Pasadena, CA 91125 (USA)
E-mail: nslewis@caltech.edu
cxx@caltech.edu

[d] I. D. Sharp
Physical Biosciences Division
Lawrence Berkeley National Laboratory
Berkeley, CA 94720 (USA)

[e] J. Jin
Engineering Division, Lawrence Berkeley National Laboratory
Berkeley, CA 94720 (USA)

[f] N. S. Lewis
Division of Chemistry and Chemical Engineering
210 Noyes Laboratory, 127-72, California Institute of Technology
Pasadena, CA 91125 (USA)

[*] Present address:
Conn Center for Renewable Energy Research
University of Louisville
Louisville, KY 40292 (USA)

Supporting Information for this article is available on the WWW under <http://dx.doi.org/10.1002/cssc.201402896>.

product crossover, both to avoid deleterious product recombination and explosive/flammable product mixtures, and to provide a facile ion-transport pathway. The electrolytes facilitate ion transport between the cathode and anode compartments. The supporting structure includes a mechanism for gathering light (e.g., window, lens arrays), input and output ports (e.g., input feedstocks, supporting electrolyte, and effluent products), and structural elements, and serves as a temporary storage space for products.

Most laboratory research has focused on the study of the intrinsic materials properties of photoelectrochemical assemblies in a half-cell configuration,^[3-11] in which the reactant/product transport is optimized by external stirring and in which any resistive losses due to solution transport in the cell are compensated by an external voltage bias. Over the last four decades, a variety of full-cell demonstrations have been reported, though reports of robust product separation and collection are rare.^[12-21] A construct that can lead to a deployable and scalable solar fuels-generation system must, however, include not only the active light-absorbing, electrocatalytic and electrolyte components, but also a chassis to synergistically integrate the cathode, anode, and membrane separator, and maintain the optimal and safe operation of these individual components.

The operational conditions and constraints for an efficient, stable, and scalable solar-hydrogen generator have been provided by prior modeling and simulation studies.^[21-26] Specifically, the geometric parameters of various cell designs, the optimal band gap combination for photoabsorbers, the overall kinetic overpotentials for electrocatalysts, the permeability and conductivity properties for membrane separators, and the conductivity and pH requirements for the solution electrolyte for a solar-driven water-splitting system have been evaluated in detail.^[22,23,27-30] In particular, to construct a solar-driven water-splitting prototype that robustly separates the reaction products to avoid hazardous gas mixtures (4 vol.% flammable limit of H₂ in air), either a cation-exchange membrane or an anion-exchange membrane is required to prevent the diffusive and convective crossover of products between the cathode and anode chamber. As a result, acidic or alkaline solutions are required to minimize the transport loss through the membrane separator, because of the very small transference number for the active species in ion exchange membranes under near-neutral pH conditions. Moreover, modeling/simulation and experimental demonstrations have shown that significant voltage losses occur under operation at near-neutral pH in buffered solutions in the bulk of the electrolyte, due to the pH gradients that form at the surface of the photoelectrodes even when the cell dimensions are optimized.^[31]

The requirements of operating in acidic or alkaline solutions limit many options for suitable materials choices for the system components. For instance, efficient photoabsorbers that are used in photovoltaic applications, such as GaAs, CdTe, CuInGaSe₂, etc, would dissolve and corrode quickly in contact with an electrolyte solution near pH 0 or 14. We therefore focused on materials that are intrinsically stable in strong acidic solution, such as WO₃ and Si for photoanode and photocathode, respectively. Although the wide band gap of WO₃ (2.6–

2.7 eV.^[10,11]) will limit the solar-to-hydrogen conversion efficiency, η_{STH} , of this proof-of-concept demonstration system, WO₃ is one of a few metal oxides that exhibits long-term stability under acidic conditions.^[10] To provide sufficient voltage to drive the water-splitting reaction, a two junction (2 J) crystalline silicon substrate was connected in series with the WO₃ and overall water splitting was achieved under dual-side simulated 1 sun illumination (200 mWcm⁻²). The whole system was formed by integration of the WO₃, 2 J Si and a Nafion membrane into a louvered configuration, for which the geometric parameters of the design, such as the tilt angle, channel height and membrane height were optimized by use of a multi-physics model that accounted for light absorption, electron and ion transport and product crossover of the system under consideration. The photoelectrochemical performance of the photocathode, photoanode and the integrated device were also evaluated experimentally and used in conjunction with modeling and simulation to formulate predictions of the behavior of the whole system that were then confirmed by experimental observations of the system performance.

Results and Discussions

Optimal Geometric Parameters in the Louvered Design

The overall solar-to-hydrogen (STH) conversion efficiency, η_{STH} , in a fully integrated system is dependent on the detailed device configuration as well as on the performance characteristics of individual components that include photoabsorbers, electrocatalysts, electrolytes, and membrane separators. The goal of optimizing a specific system construct is to produce a detailed geometric design space within which the η_{STH} approaches the theoretical limit of the conversion efficiency based solely on the intrinsic materials properties of the system components.

Figure 1 shows the cross-sectional schematic illustration of the louvered system design, in which the photoelectrochemical (PEC) assemblies were interconnected and separated by membrane separators. The PEC assembly formed a tilt angle, θ , with respect to the horizontal axis. The membrane separator was vertically oriented and was parallel to the direction of the illumination, to maximize the light-absorption area in the PEC assemblies. Electrolyte inlets and outlets and the product-gas outlets were located at the top and bottom of the anode and cathode chambers, respectively. The channel on the top and the bottom of each louver was designed to reduce the resistive loss between the cathode and anode compartments. Figure 1 also presents a detailed construct of the PEC assembly, in which a tandem photoabsorber that contained a top cell and a bottom cell was coated by a transparent conductive oxide (TCO) layer as well as by an electrocatalyst layer for the oxygen-evolution reaction (OER) or hydrogen-evolution reaction (HER).

Using the state-of-the-art electrocatalysts in 1.0 M H₂SO₄, Figure 2 shows the optimal solar-to-hydrogen efficiency, $\eta_{\text{STH,opt}}$, as a function of the band gap combination of the tandem pho-

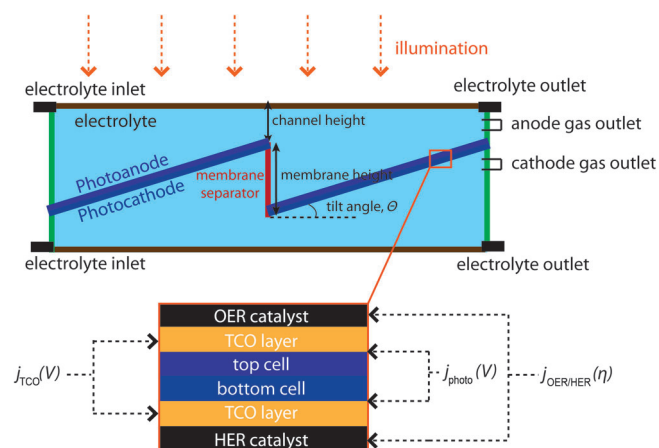


Figure 1. Schematic illustration of the device construct of the louvered-design solar-hydrogen device.

toabsorbers at Schottky-Queisser limit, in which no potential loss was accounted for due to ionic transport losses in an actual system design. The maximum $\eta_{\text{STH,opt}}$ that is, $\eta_{\text{STH,opt,max}}$ of 31.3% was calculated at a band-gap combination of 1.6 eV/0.9 eV, and represents the maximum attainable efficiency for such a solar-driven water-splitting system without any losses due to solution-based or membrane-based transport. The detailed current density distribution along the photoelectrode, which could produce significant kinetic overpotential due to high operational current densities at the edge of the electrode, was also not accounted for in this 0-dimensional calculation.

The goal of the optimization of the geometric parameters in the louvered design is to establish a design space in which η_{STH} of a realistic prototype can in practice approach $\eta_{\text{STH,opt}}$. Figure 2b shows the effective STH conversion efficiency, $\eta_{\text{STH,eff}} = \eta_{\text{STH}} A_{\text{illumination}}/A_{\text{electrode}}$ and $\eta_{\text{STH,eff}}/\eta_{\text{STH,opt}}$ as a function of the tilt angle for five different membrane heights in the louvered design, where $A_{\text{illumination}}$ and $A_{\text{electrode}}$ are the projected illumination area and the electrode area, respectively. The band-gap combination for the tandem absorber was set to 1.6 eV/

0.9 eV. The channel height was set to 5 mm because η_{STH} exhibited a very weak dependence on channel height when the channel height was larger than 5 mm (data not shown). Even with the smallest cell dimensions, the decrease of η_{STH} due to product-gas crossover in the louvered design was negligible (<0.5%), due to the use of a membrane separator.

At a given membrane height, when the tilt angle decreased, the electrode length increased and the pathways between the mid-point of the cathode and the mid-point of the anode also increased, which resulted in additional potential loss and thus a decrease in the resulting system efficiency. However, as the tilt angle decreased, the current density that was normalized to the electrode area, J_{norm} , also increased and followed a $\cos(\theta)$ dependence. As a result, the maximum effective STH conversion efficiency was obtained at 5.5°, 9.5°, 15°, 16.5°, 19°, and 22.5° for membrane heights of 1 mm, 4 mm, 10 mm, 12 mm, and 20 mm, respectively. The allowable geometric parameters in the louvered design are plotted in Figure 2b. For instance, to achieve 90% of $\eta_{\text{STH,opt,max}}$ the membrane height cannot exceed 15 mm even at the optimal tilt angle.

Experimental Construction of the Louvered Design

Due to the highly corrosive operational environment in 1.0 M HClO_4 , Si-based photocathode materials and WO_3 -based photoanode materials were used to achieve cell stability. Figure 3a shows an exploded view of the prototype and general assembly. The prototype PEC solid model was designed using SolidWorks (Waltham, Massachusetts). The prototype consisted of: 2×PEC assemblies (16.1×44.0 mm), 1×Nafion membrane (3×44 mm), 2×acrylic chassis that were 3-D printed, 2×glass windows (50×60×1 mm), 8×inlet and outlet ports (PEEK, ID 0.75 mm, OD 1.5875 mm), and 16×bolts (2-56" x 1") and/or epoxy (Loctite 9460, Hysol). Figure 3b shows a cross-sectional schematic of the monolithically integrated photoelectrode assembly. The photocathode consisted of a Pt/ $\text{TiO}_2/\text{n}^+\text{p}$ Si electrode and the photoanode consisted of a $\text{WO}_3/\text{p}^+\text{n}$ -Si electrode. Two solid-state Si junctions were employed collectively

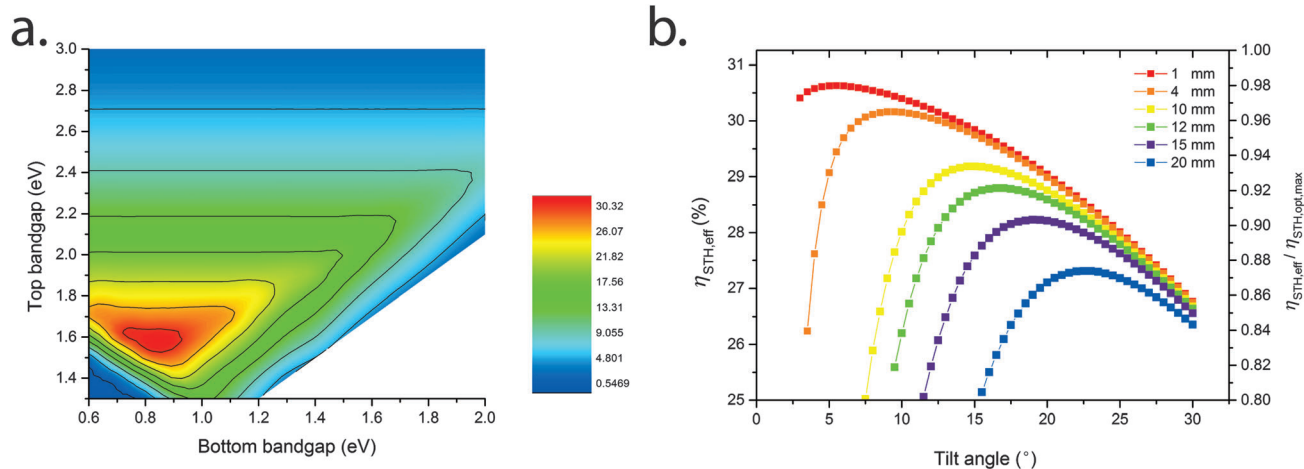


Figure 2. (a) $\eta_{\text{STH,opt}}$ as a function of the band-gap combinations of the tandem photoabsorber. (b) $\eta_{\text{STH,eff}}$ (left axis) and $\eta_{\text{STH,eff}}/\eta_{\text{STH,opt,max}}$ (right axis) as a function of the tilt angle in the louvered design, where the membrane height was set to 1 mm, 4 mm, 10 mm, 12 mm, or 20 mm.

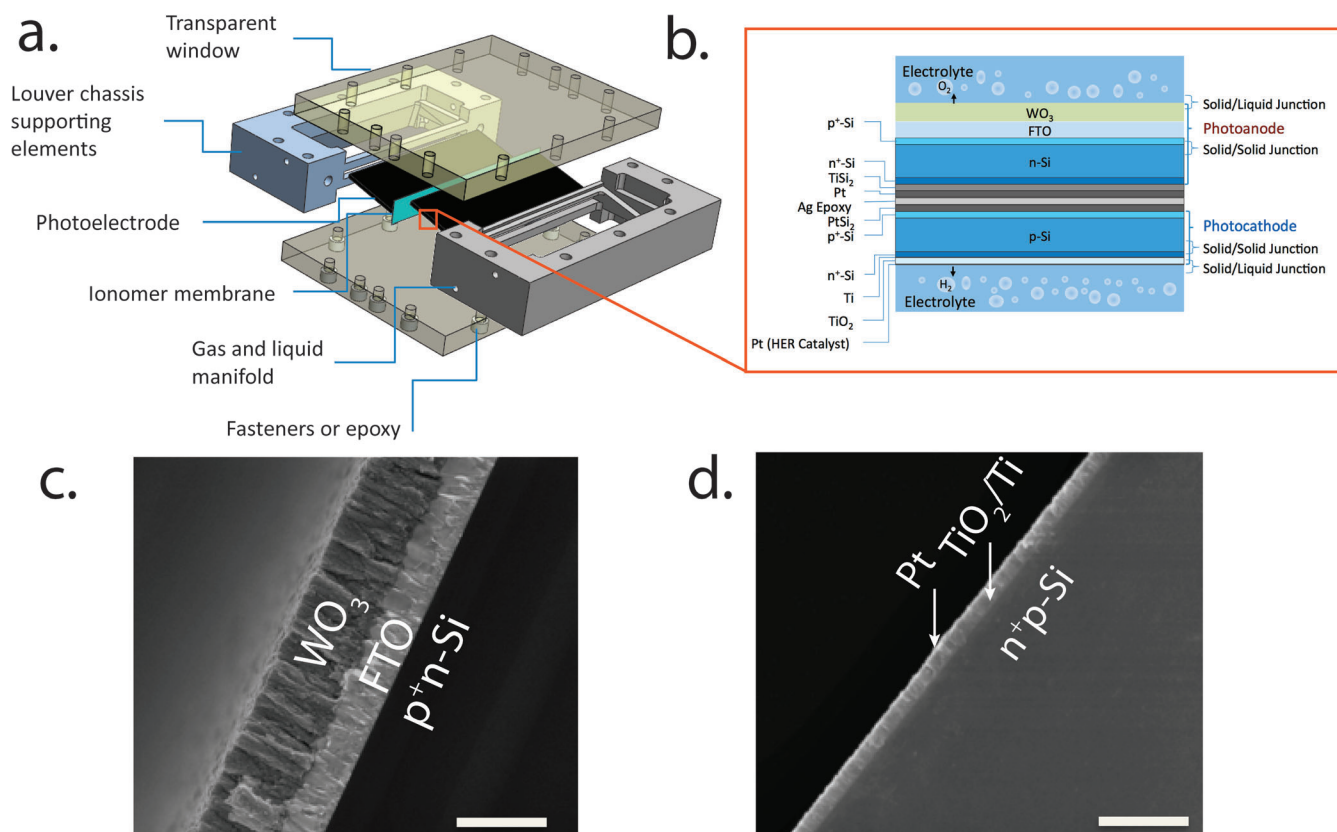


Figure 3. (a) The exploded view of the CAD model for the louvered design; (b) a cross-sectional schematic of the monolithically integrated photoelectrode assembly; (c) and (d) cross-sectional scanning electron micrographs of the photoanode assembly ($\text{WO}_3/\text{FTO}/\text{p}^+\text{n-Si}$) and photocathode assembly ($\text{Pt}/\text{TiO}_2/\text{Ti}/\text{n}^+\text{p-Si}$), respectively. The inset scale bar is $1\ \mu\text{m}$.

in the photocathode and the photoanode to overcome the thermodynamic voltage and kinetic overpotentials of the water-splitting reaction. Figure 3c and 3d show the cross-sectional SEM images of the photoanode and the photocathode. The FTO layer prepared by spray pyrolysis and the WO_3 layer prepared by sputtering in the photoanode exhibited uniform thickness across the crystalline Si substrates. The thin, transparent Pt layer in the photocathode formed discontinuous metal islands on the Ti/TiO_2 layer and was observable due to the production of a prominent contrast in SEM images.

Device Performance and Model Validation

The performance characteristics of the photocathode and photoanode were separately determined in a traditional three-electrode PEC cell. After a short stabilization period, the current-voltage characteristic of the photoelectrodes reached a steady state. Figure 4a and 4b show the current density as a function of potential vs. the reversible hydrogen electrode (RHE) after 120 h of cyclic voltammetric scans of the photocathode and photoanode, respectively. The photocathode exhibited an open-circuit voltage of 490 mV and a current density of $19.34\ \text{mA cm}^{-2}$ at the formal potential for H_2 evolution, $E^\circ(\text{H}_2\text{O}/\text{H}_2)$, whereas the photoanode exhibited an open-circuit voltage of 990 mV and a current density of $1.24\ \text{mA cm}^{-2}$ at $E^\circ(\text{O}_2/\text{H}_2\text{O})$. Due to the high band gap of WO_3 , the overall device effi-

ciency was limited by the low photocurrent density in the photoanode. The performance of the full system was measured by determination of the rates of hydrogen and oxygen production in the cathode and anode chamber, respectively (Figure 4c). After an initial stabilization period, the average rate of hydrogen production was $0.17\ \text{mL h}^{-1}$, which corresponded to an operating current density of $0.39\ \text{mA cm}^{-2}$ and η_{STH} of 0.24% for $> 20\ \text{h}$ of operation under dual-side simulated 1 sun illumination (i.e., a total of $200\ \text{mW cm}^{-2}$).

To fully understand the cell performance and also to validate the modeling and simulation tools, the performance of the integrated louvered device was simulated by a multiphysics model that accounted for the electronic and ionic transport in the system. Figure 5a shows the electrolyte potential-distribution profile for the louvered design that was experimentally constructed and tested. Using the current-voltage relationships determined experimentally from the three-electrode measurements, the simulation yielded a calculated η_{STH} of 0.235%, in excellent agreement with the experimental observations for the operating system. Figure 5b and 5c depict the operational current density and the resistive loss along the electrode width. The asymmetry of the current density distribution originated from the asymmetry in the pathways for proton conduction between the cathode and the anode. Due to the low operational current density, the maximum resistive loss in the louvered design was less than 5 mV, which resulted

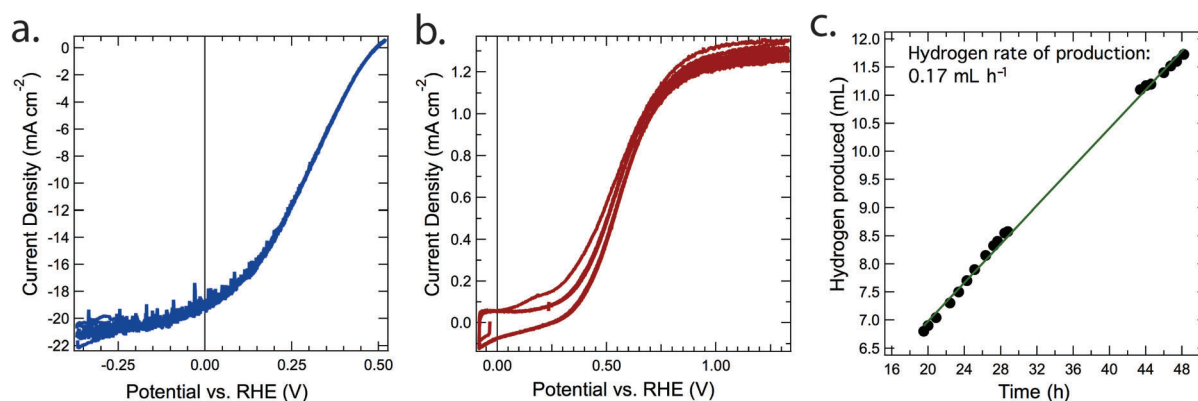


Figure 4. Current density as a function of potential for the Pt/TiO₂/Ti/n⁺ p Si photocathode (a) and for the WO₃/FTO/p⁺ n Si photoanode (b) in aqueous 1.0 M HClO₄ under simulated 1 sun illumination after 120 h of cyclic voltammetry scans. (c) Rate of production of hydrogen gas in the cathode compartment. The average rate of H₂ production after a stabilization period was calculated to be 0.17 mL h⁻¹ from a linear fit of the experimental data.

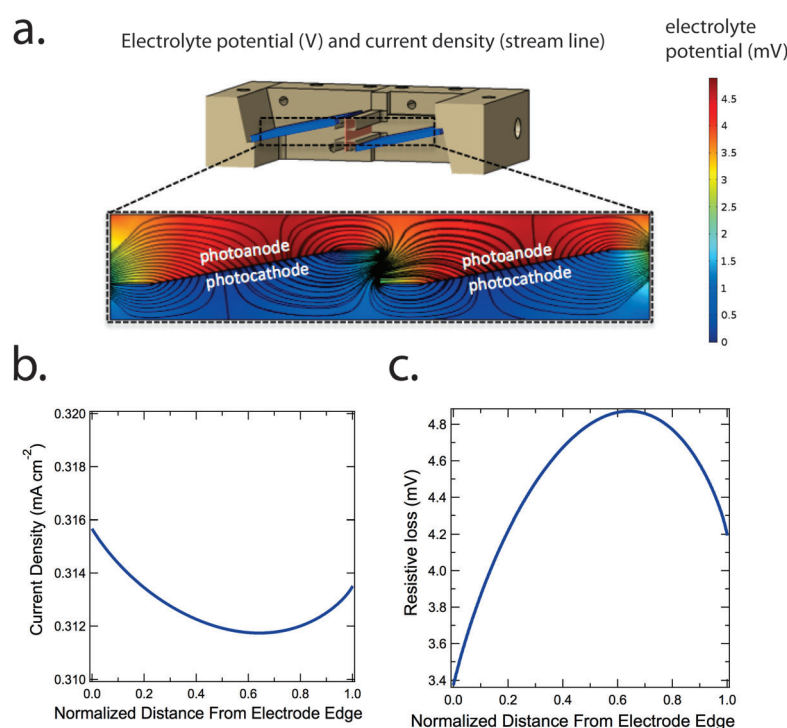


Figure 5. (a) Electrolyte potential-distribution profile for the louvered design that was experimentally constructed and tested. Current density (b) and resistive loss (c) as a function of the normalized distance from the photoelectrode edge obtained from the modeling and simulation.

in a relatively uniform current distribution (0.313 ± 0.002 mA cm⁻²) along the electrode width. At the operating current density, the photocathode operated at a potential that was close to its open-circuit voltage (490 mV) and the rest of the photovoltage (~ 740 mV) that drove the entire water-splitting reaction was provided by the photoanode.

The low operating current density of this particular PEC assembly resulted in minimal voltage penalty from the resistive loss in the solution, and significantly relaxed the requirements for the electrode dimensions and membrane dimensions. If instead, a highly efficient PEC assembly were incorporated into the system, a significantly higher average photocurrent density

along the electrode would be produced. This higher photocurrent density ($10\text{--}20$ mA cm⁻²) would then result in a larger resistive loss and a larger voltage penalty due to the increased pH gradients at the surface of the electrode at high ionic fluxes. Modeling/simulation and experimental measurements have shown significant voltage losses due to pH gradients for cells operating with bulk electrolytes at near-neutral pH, even with highly buffered solutions at moderately low current densities (< 5 mA cm⁻²).^[31] Such systems can yield high rates of water-splitting at a given illumination intensity especially in the presence of significant convection and with no pressure drop that in practice would be required for the beneficial collection of the H₂(g) while separating it acceptably from the evolved O₂(g). However, the instantaneous solar-to-

hydrogen efficiencies of such systems cannot be compared to the steady-state efficiencies of systems that are intrinsically safe and do not produce potentially explosive mixtures of H₂(g) and O₂(g). For example, use of a membrane separator in solar-driven water-splitting systems based on buffered neutral-pH solutions has been shown to result in large pH gradients near the electrodes, electrodiffusion of the buffer anions in the solution, and very low ($< 0.1\%$) η_{STH} values even for photoabsorber/electrocatalyst devices that by themselves exhibit $> 7\%$ solar-energy conversion efficiencies.^[31] As shown in Figure 2, in conjunction with use of a strongly acidic solution (1.0 M HClO₄) and a membrane separator, the louvered design with opti-

mized cell dimensions exhibited minimal voltage penalty due to the resistive loss in the solution and the pH gradients at the surface of the electrode, was intrinsically safe, and exhibited minimal efficiency loss due to product crossover, even when the photocurrent density was as high as 25 mA cm^{-2} .

Experimental Section

Multiphysics Modeling and Simulation

Boundary conditions for the louvered design: Figure 1 presents a detailed setup, with color coding, for the boundary conditions used in the simulations. Symmetry boundary conditions for the current densities were employed at the two vertical walls (green). Insulating boundary conditions were applied at the upper and bottom bounds of the cell (brown). For optimization of the geometric dimensions of the electrode, a Neumann (or second-type) boundary condition of the current flux as a function of the operational voltage ($J_{\text{photo}}(\text{V})$) was applied at the photoelectrode/TCO interface, while for understanding the cell performance with experimental materials assemblies, numerical current-voltage data were employed as the boundary conditions for the photocathode and photoanode electrodes, respectively.

Photoabsorbers: In the simulation of the optimized solar-to-hydrogen (STH) conversion efficiency, $\eta_{\text{STH,opt}}$ for the louvered system design, the numerical relationship between the current density and the operating voltage of a tandem photoabsorber was obtained from a detailed balance calculation^[32] and was then fitted using Equation (1) for an ideal diode,

$$J = J_{\text{ph}} - J_0 \left[\exp\left(\frac{eV}{\gamma kT}\right) - 1 \right], \quad (1)$$

where J_{ph} is the photocurrent density, J_0 is the reverse saturation current density, and γ is the diode ideality factor. The photoelectrodes were tilted at an angle, θ , with respect to the horizontal axis, and the resulting current density that was normalized to the electrode area, J_{norm} was given by:

$$J_{\text{norm}} = \frac{A_{\text{illumination}}}{A_{\text{electrode}}} \times J_{\text{ph}} - J_0 \left[\exp\left(\frac{eV}{\gamma kT}\right) - 1 \right] \quad (2)$$

where $A_{\text{illumination}}$ and $A_{\text{electrode}}$ are the projected illumination area and the electrode area, respectively. In the simulation of the WO_3/Si -based photoelectrochemical assembly, the experimental current density-voltage characteristic was employed as a boundary condition for the behavior of the tandem photoabsorber.

Electrocatalysts: The current density, $j_{\text{OER/HER}}$ as a function of the overpotential, η , for the OER and HER, respectively, can be described by the Butler–Volmer equation.^[33]

$$j_{\text{OER/HER}} = j_{0,\text{OER/HER}} \left[\exp\left(\frac{\alpha_{\text{a,OER/HER}} F \eta}{RT}\right) - \exp\left(\frac{\alpha_{\text{c,OER/HER}} F \eta}{RT}\right) \right] \quad (3)$$

where $j_{0,\text{OER/HER}}$ is the exchange-current density for OER or HER, respectively, and $\alpha_{\text{a,OER/HER}}$ and $\alpha_{\text{c,OER/HER}}$ are the anodic and cathodic

Table 1. Fundamental parameters used in the calculation of the limiting efficiency.^[34]

Electrochemical kinetics		Operating conditions	
OER exchange current density, $i_{0,\text{OER}}$	$0.00014 \text{ mA cm}^{-2}$	temperature, T	300 K
OER anodic transfer coefficient, $\alpha_{\text{a,OER}}$	1	solar concentration, C	1 sun (100 mW cm^{-2})
OER cathodic transfer coefficient, $\alpha_{\text{c,OER}}$	0.1		
HER exchange current density, $i_{0,\text{HER}}$	1 mA cm^{-2}		
HER anodic transfer coefficient, $\alpha_{\text{a,HER}}$	2.57		
HER cathodic transfer coefficient, $\alpha_{\text{c,HER}}$	2.57		
thermodynamic potential, φ_0	1.23 V		

transfer coefficients for the OER or the HER, respectively. The exchange-current density and the transfer coefficient were obtained by fitting the current-voltage relationship of state-of-the-art electrocatalysts (IrO_x for OER and Pt for HER in $1 \text{ M H}_2\text{SO}_4$).^[34] Note that kinetic parameters of electrocatalysts in $1 \text{ M H}_2\text{SO}_4$ were used in the simulation due to the lack of experimental data for IrO_x and Pt in 1 M HClO_4 . Table 1 lists the parameters applied in the calculations.

Membrane separators, transparent conductive oxide (TCO) layer and solution electrolyte: The electron transport in the TCO layer and the ion transport in the membrane separators (Nafion) as well as in the solution electrolyte (1.0 M HClO_4) were modeled using Ohm's law:

$$j_{\text{el,mem,TCO}} = -\sigma_{\text{el,mem,TCO}} \nabla \varphi_{\text{el,mem,TCO}} \quad (4)$$

where $\sigma_{\text{el,mem,TCO}}$ is the conductivity of the electrolyte, the membrane (Nafion), or the TCO layer, respectively, $\nabla \varphi_{\text{el,mem,TCO}}$ is corresponding potential drop, and $j_{\text{el,mem,TCO}}$ is the corresponding current density. The ionic conductivities of the Nafion film, the electrolyte ($1.0 \text{ M perchloric acid}$) and the TCO layer were taken to be 10 S m^{-1} , 40 S m^{-1} , and 10^5 S m^{-1} , respectively.

Operating principles of device efficiency: The η_{STH} was defined as:

$$\eta_{\text{STH}} = \frac{J \cdot \varphi_0}{P} \eta_{\text{F}} \eta_{\text{pc}}, \quad (5)$$

where J is the current density output from the device, φ_0 is the equilibrium potential of the electrochemical reaction, P is the input power of the solar energy, η_{F} is the Faradaic efficiency of the electrode reaction, and η_{pc} is the product-collection efficiency. The value of η_{F} was set to unity in the model, while η_{pc} was defined by the following equation:

$$\eta_{\text{pc}} = \frac{\int_{A_{\text{a/c}}} j \text{d}A - \int_{A_{\text{sep}}} n F N_{\text{fuel}} \text{d}A}{\int_{A_{\text{a/c}}} j \text{d}A}, \quad (6)$$

where j is the current density at the interfaces between the catalysts and the solution, the net reaction current, N_{fuel} represents the current lost due to diffusive crossover of hydrogen from the cathode to the anode chamber, n is number of electrons transferred (2 for the HER and 4 for the OER), and $A_{\text{a/c}}$ and A_{sep} are the electrode area and the Nafion area that separate the anodic and cathodic chambers, respectively.

Photoanode Fabrication

The raw materials used in this study and the Si wafer processing and junction fabrication are described in the Supporting Informa-

tion. To ensure an ohmic contact and to improve the lateral conductivity between the WO_3 and the p^+ emitter, a thin film of fluorine-doped tin oxide (FTO) was deposited by spray pyrolysis. The Si wafer was etched in a buffered HF solution to remove the surface oxide prior to deposition of the FTO. The Si wafer was then heated to 490°C and was exposed to a solution comprised of 0.033 M of NH_4F , 15.45 M of ethanol, 0.42 M butyltin trichloride, and 1.36 M of water, until the sheet resistance was less than $<100\ \Omega\text{sq}^{-1}$ across a $4''$ diameter Si wafer. The WO_3 layer was deposited by radio-frequency (RF) sputtering of W onto the FTO-coated Si wafers in a 9-gun confocal system (AJA international) with a base pressure of 1×10^{-8} Torr.

Deposition was performed at a substrate temperature of 300°C and at an Ar and O_2 partial chamber pressure of 3.4 mTorr and 1.6 mTorr , respectively. The RF power was set to 150 W across a 0.05 m diameter W (99.9995%) target, with a rate of deposition of 12.5 nm min^{-1} . The sample was cooled to 50°C prior to removal from the sputtering chamber. To improve the photoelectrochemical performance, the produced WO_3/Si assembly was annealed in air for 2 h at 400°C .

Photocathode Fabrication

The photocathode was fabricated by depositing a Ti/ TiO_2 layer and a transparent Pt layer, respectively, onto the n^+pp^+ Si wafer. Prior to the Ti/ TiO_2 deposition, the substrate was etched in buffered HF solution for 1 min and was sputtered at 15 W for 10 min in an Ar plasma at 20 mTorr . To promote the adhesion between the TiO_2 and the Si wafer, a 5 nm layer of titanium (99.995% pure) was sputtered at 23.87 Wcm^{-2} at an Ar pressure of 1.8 mTorr .^[18] The TiO_2 layer was sputtered at 23.87 Wcm^{-2} at an O_2 chamber pressure of 1.9 mTorr . A nominally 5 nm thick layer of Pt (99.99%) was deposited at 23.87 Wcm^{-2} with an Ar chamber pressure of 2 mTorr .

Cell operation and gas collection

The current density vs. potential (J - E) photoelectrochemical measurements for all photoelectrodes were obtained in stirred solutions of 1.0 M HClO_4 (Sigma Aldrich, 60%) that were made with deionized MilliQ water ($>18\text{ Mohm cm}$ resistivity). For the half-cell measurements, the photoelectrode was the working electrode and Pt gauze was the counter electrode, with the Pt separated from the main cell by a glass frit. The reference electrode was a Ag/AgCl (BASi) electrode in a solution saturated with potassium chloride. The cell was constructed of glass and had a flat quartz window. Electrochemical data were collected using a Bio-Logic SP-200 potentiostat.

To measure the production rates of hydrogen and oxygen, inverted burettes filled with water were used to determine the water volume displaced by the generated gases (hydrogen and oxygen) as a function of time. The rate of gas production was converted to an equivalent current density using Faraday's law combined with the ideal gas law. The relationship was separately verified experimentally with an electrolyzer and gas-collection burettes. Accurate $\text{O}_2(\text{g})$ production rates were difficult to obtain due to the low $\text{O}_2(\text{g})$ production rate and the parasitic absorption of $\text{O}_2(\text{g})$ onto the internal surface of the chassis and the epoxy materials that were used in the prototype construction. However, quantitative measurements of the oxygen production of the photoanode were carried out (see Supporting Information, Figure S1) and stable production of oxygen at close to 100% faradic efficiency of the OER at the photoanode materials assembly was observed. The purity of the collected gas products was verified with a two-channel gas

chromatographic analyzer (Agilent, 7890 A Santa Clara, CA), one channel for analysis of H_2 and the other for analysis of O_2 . Standards were run throughout the experiments to verify the composition of the gas samples.

Conclusions

A fully integrated, acid-stable and scalable louvered operational solar-driven water-splitting system has been modeled numerically and constructed experimentally. The louvered design maximized the area for light absorption and also provided necessary pathways for ion transport between the cathode and anode compartment. The optimal geometric parameters for the louvered design were provided by a multi-physics model in which the η_{STH} in a realistic prototype, that accounted for solution transport losses and product-crossover losses, approached the optimal solar-conversion efficiency at the detailed-balance limit. The voltage losses associated with ion transport as well as due to any pH gradients at the surface of the electrodes, and the efficiency loss associated with product crossover, were minimized by the use of a strongly acidic solution and a membrane separator. Using $\text{WO}_3/\text{FTO}/\text{p}^+\text{n}$ Si as the photoanode, $\text{Pt}/\text{TiO}_2/\text{Ti}/\text{n}^+\text{p}$ Si as the photocathode, and a Nafion membrane separator, η_{STH} of 0.24% was demonstrated in 1.0 M H_2SO_4 for $>20\text{ h}$ of continuous operation under dual-side illumination (200 mWcm^{-2}) with minimal product crossover. The louvered design described herein provides a robust platform for the further implementation of various types of improved photoelectrochemical assemblies and can lead to an efficient, scalable, stable and intrinsically safe solar-driven water-splitting system.

Acknowledgements

This material is based upon work performed by the Joint Center for Artificial Photosynthesis, a DOE Energy Innovation Hub, supported through the Office of Science of the U.S. Department of Energy under Award Number DE-SC0004993.

Keywords: multi-physics modeling · prototype · solar fuels · tungsten oxide · water splitting

- [1] M. G. Walter, E. L. Warren, J. R. McKone, S. W. Boettcher, Q. X. Mi, E. A. Santori, N. S. Lewis, *Chem. Rev.* **2010**, *110*, 6446–6473.
- [2] N. S. Lewis, D. G. Nocera, *Proc. Natl. Acad. Sci. USA* **2007**, *104*, 20142–20142.
- [3] S. W. Boettcher, J. M. Spurgeon, M. C. Putnam, E. L. Warren, D. B. Turner-Evans, M. D. Kelzenberg, J. R. Maiolo, H. A. Atwater, N. S. Lewis, *Science* **2010**, *327*, 185–187.
- [4] K. Keis, E. Magnusson, H. Lindstrom, S. E. Lindquist, A. Hagfeldt, *Sol. Energy Mater. Sol. Cells* **2002**, *73*, 51–58.
- [5] G. M. Wang, H. Y. Wang, Y. C. Ling, Y. C. Tang, X. Y. Yang, R. C. Fitzmorris, C. C. Wang, J. Z. Zhang, Y. Li, *Nano Lett.* **2011**, *11*, 3026–3033.
- [6] A. Paracchino, V. Laporte, K. Sivula, M. Gratzel, E. Thimsen, *Nat. Mater.* **2011**, *10*, 456–461.
- [7] A. B. Murphy, P. R. F. Barnes, L. K. Randeniya, I. C. Plumb, I. E. Grey, M. D. Horne, J. A. Glasscock, *Int. J. Hydrogen Energy* **2006**, *31*, 1999–2017.
- [8] K. Sivula, R. Zboril, F. Le Formal, R. Robert, A. Weidenkaff, J. Tucek, J. Frydrych, M. Gratzel, *J. Am. Chem. Soc.* **2010**, *132*, 7436–7444.

- [9] D. K. Zhong, J. W. Sun, H. Inumaru, D. R. Gamelin, *J. Am. Chem. Soc.* **2009**, *131*, 6086–6087.
- [10] Q. X. Mi, A. Zhanaidarova, B. S. Brunshwig, H. B. Gray, N. S. Lewis, *Energy Environ. Sci.* **2012**, *5*, 5694–5700.
- [11] J. M. Spurgeon, J. M. Velazquez, M. T. McDowell, *Phys. Chem. Chem. Phys.* **2014**, *16*, 3623–3631.
- [12] O. Khaselev, J. A. Turner, *Science* **1998**, *280*, 425–427.
- [13] S. Y. Reece, J. A. Hamel, K. Sung, T. D. Jarvi, A. J. Esswein, J. J. H. Pijpers, D. G. Nocera, *Science* **2011**, *334*, 645–648.
- [14] R. E. Rocheleau, E. L. Miller, A. Misra, *Energy Fuels* **1998**, *12*, 3–10.
- [15] K. Fujii, S. Nakamura, M. Sugiyama, K. Watanabe, B. Bagheri, Y. Nakano, *Int. J. Hydrogen Energy* **2013**, *38*, 14424–14432.
- [16] S. Licht, B. Wang, S. Mukerji, T. Soga, M. Umeno, H. Tributsch, *J. Phys. Chem. B* **2000**, *104*, 8920–8924.
- [17] N. A. Kelly, T. L. Gibson, *Int. J. Hydrogen Energy* **2006**, *31*, 1658–1673.
- [18] B. Seger, T. Pedersen, A. B. Laursen, P. C. K. Vesborg, O. Hansen, I. Chorkendorff, *J. Am. Chem. Soc.* **2013**, *135*, 1057–1064.
- [19] F. F. Abdi, L. H. Han, A. H. M. Smets, M. Zeman, B. Dam, R. van de Krol, *Nat. Commun.* **2013**, *4*, 2195.
- [20] F. Zhu, J. Hu, I. Matulionis, T. Deutsch, N. Gaillard, A. Kunrath, E. Miller, A. Madan, *Philos. Mag.* **2009**, *89*, 2723–2739.
- [21] E. S. Smotkin, S. Cerveramarch, A. J. Bard, A. Campion, M. A. Fox, T. Mal-louk, S. E. Webber, *J. Phys. Chem.-Us.* **1987**, *91*, 6–8.
- [22] S. Haussener, S. Hu, C. Xiang, A. Z. Weber, N. Lewis, *Energy Environ. Sci.* **2013**, *6*, 3605–3618.
- [23] S. Haussener, C. X. Xiang, J. M. Spurgeon, S. Ardo, N. S. Lewis, A. Z. Weber, *Energy Environ. Sci.* **2012**, *5*, 9922–9935.
- [24] H. Doscher, J. Geisz, T. Deutsch, J. A. Turner, *Energy Environ. Sci.* **2014**, in press.
- [25] L. C. Seitz, Z. B. Chen, A. J. Forman, B. A. Pinaud, J. D. Benck, T. F. Jaramillo, *ChemSusChem* **2014**, *7*, 1372–1385.
- [26] S. Cervera-March, E. S. Smotkin, A. J. Bard, A. Campion, M. A. Fox, T. Mal-louk, S. E. Webber, J. M. White, *J. Electrochem. Soc.* **1988**, *135*, 567–573.
- [27] S. Hu, C. X. Xiang, S. Haussener, A. D. Berger, N. S. Lewis, *Energy Environ. Sci.* **2013**, *6*, 2984–2993.
- [28] C. Xiang, Y. Chen, N. S. Lewis, *Energy Environ. Sci.* **2013**, *6*, 3713–3721.
- [29] Y. K. Chen, C. X. Xiang, S. Hu, N. S. Lewis, *J. Electrochem. Soc.* **2014**, *161*, 1101.
- [30] M. R. Singh, C. Xiang, N. S. Lewis, **2014**, unpublished results.
- [31] J. Jin, K. Walczak, M. R. Singh, C. Karp, N. S. Lewis, C. X. Xiang *Energy Environ. Sci.* **2014**, DOI: 10.1039/C4EE01824A.
- [32] W. Shockley, H. J. Queisser, *J. Appl. Phys.* **1961**, *32*, 510.
- [33] A. J. Bard, L. R. Faulkner, *Electrochemical Methods, Fundamentals and Ap-plications*, Wiley, **2000**.
- [34] C. C. L. McCrory, S. H. Jung, J. C. Peters, T. F. Jaramillo, *J. Am. Chem. Soc.* **2013**, *135*, 16977–16987.

Received: August 26, 2014

Published online on January 7, 2015